Electronic supplementary information

Crystalline to Amorphous Transformation in Solid-Solution Alloy Nanoparticles Induced by Boron Doping

Keigo Kobayashi,[a] Kohei Kusada,[a] Dongshuang Wu,[a] Naoki Ogiwara,[a,+] Hirokazu Kobayashi,[a,b] Mitsutaka Haruta,[c] Hiroki Kurata,[c] Satoshi Hiroi,[d,e] Okkyun Seo,[d,f] Chulho Song,[f] Yanna Chen,[d,f] Jaemyung Kim,[f] Akhil Tayal,[f] Osami Sakata,[d,e,f,g] Koji Ohara,[e] Tetsuo Honma,[e] Hiroshi Kitagawa*[a,h,i]*

a. Division of Chemistry, Graduate School of Science, Kyoto University, Kitashirakawa-Oiwakecho, Sakyo-ku, Kyoto 606-8502, Japan

b. JST, PRESTO, 4-1-8 Honcho, Kawaguchi, Saitama, 332-0012, Japan.

c. Institute for Chemical Research, Kyoto University, Gokasho, Uji, Kyoto 611-0011, Japan

d. Synchrotron X-ray Group, Research Centre for Advanced Measurement and Characterization, National Institute for Materials Science (NIMS), 1-1-1 Kouto, Sayo-cho, Sayo-gun Hyogo 679-5148, Japan

e. Japan Synchrotron Radiation Research Institute, 1-1-1 Kouto, Sayo-cho, Sayo-gun, Hyogo 679-5198, Japan.

f. Synchrotron X-ray Station at SPring-8, NIMS, 1-1-1 Kouto, Sayo-gun, Hyogo 679-5148, Japan

g. Department of Materials Science and Engineering, School of Materials and Chemical Technology, Tokyo Institute of Technology, Yokohama 226-8502, Japan

h. INAMORI Frontier Research Centre, Kyushu University, Motooka 744, Nishi-ku, Fukuoka 819-0395, Japan

i. Institute for Integrated Cell-Material Sciences (iCeMS), Kyoto University, Yoshida, Sakyo-ku, Kyoto, 606-8501, Japan.

+ Current address: Department of Basic Science, School of Arts and Sciences, The University of Tokyo, 3-8-1 Komaba, Meguro-ku, Tokyo 153-8902, Japan.

E-mail: hirokazukobayashi6@gmail.com, kitagawa@kuchem.kyoto-u.ac.jp

Experimental Procedures

Synthesis of Pd–Ru NPs: In a typical synthesis of Pd_xRu_{1-x} NPs (x = 0.5), poly(*N*-vinyl-2-pyrrolidone) (PVP, 87.2 mg, MW ≈ 55000, Aldrich) was dissolved in triethylene glycol (TEG, ca. 150 mL, TCI), and the solution was heated to 200 °C in the air with magnetic stirring. Meanwhile, $K_2[PdCl_4]$ (228.4 mg, Aldrich) and $RuCl_3 \cdot nH_2O$ (222.4 mg, Wako) were dissolved in deionized water (35 mL). The aqueous mixture solution was then slowly added to the TEG solution. The solution was maintained at 200 °C while adding the solution. After cooling to room temperature, the prepared nanoparticles were separated by centrifuging.

Synthesis of Pd–Ru–B NPs: A three-neck round-bottom flask was charged with PVP-covered Pd–Ru NPs (100 mg). The flask was purged with N_2 gas and then evacuated overnight at 80 °C to remove oxygen and moisture. The Pd–Ru–B NPs were then synthesized by adding BH_3–THF (25 mL, 1 M, Aldrich) at 80 °C under N_2 flow. After continuous stirring for 2 days, the products were collected by centrifugation. The obtained Pd–Ru–B NPs were stored at −25 °C to prevent decomposition.

X-ray fluorescence (XRF) spectroscopy: The compositions of Pd–Ru NPs were determined by XRF measurement performed by Rigaku ZSX Primus IV. The calculated composition was $Pd_{0.48}Ru_{0.52}$.

Transmission electron microscopy (TEM) images: TEM images were captured using a Hitachi HT7700 instrument operated at 100 kV accelerating voltage. The samples were dispersed in ethanol and dropped onto the thin carbon support film.

Scanning TEM (STEM) images, energy-dispersive X-ray spectroscopy (EDS)-electron-energy-loss spectroscopy (EELS) maps and selected area electron diffraction (SAED) measurement: STEM-EDS-EELS maps were captured using a JEM-ARM200F instrument equipped with a JED-2300T SDD100GV and an electron-energy-loss spectrometer (Gatan, Inc., GIF Quantum ERS). The experiments were performed at 200 kV. Fast Fourier transform (FFT) patterns of STEM images were obtained by using Gatan DigitalMicrograph software.

Powder X-ray diffraction (PXRD) measurements: The structures of Pd–Ru and Pd–Ru–B NPs were investigated by powder XRD analysis using a Bruker D8 Advance diffractometer (Cu $K\alpha$ radiation).

High energy X-ray diffraction (HEXRD) measurements: HEXRD measurements for Pd–Ru and Pd–Ru–B NPs were performed at the BL04B2 beamline in SPring-8, Japan. The NP samples were loaded in a quartz glass capilary with 1.0 mm diameter. The irradiated X-ray beam was monochromated by a

Si(220) reflection on a bent single-crystalline Si monochromator. The incident X-ray energy was 61.377 keV (λ = 0.20207 Å), and the measurement angle was from 0.3 to 49°. The scattered intensity was detected by a six-detector system consisting of four CdTe detectors for lower angles and two high-purity Ge detectors for higher angles. During the measurement for Pd–Ru–B NPs, a cryostat was used to maintain a low temperature of 233 K, whereas the measurement for Pd–Ru NPs was performed at room temperature.

X-ray absorption fine structure (XAFS) measurements: X-ray absorption spectra (XAS) were collected at the BL14B2 beamline, SPring-8 in transmission mode under ambient conditions using a Si (311) double crystal monochromator.

Results and Discussion

1. TEM images

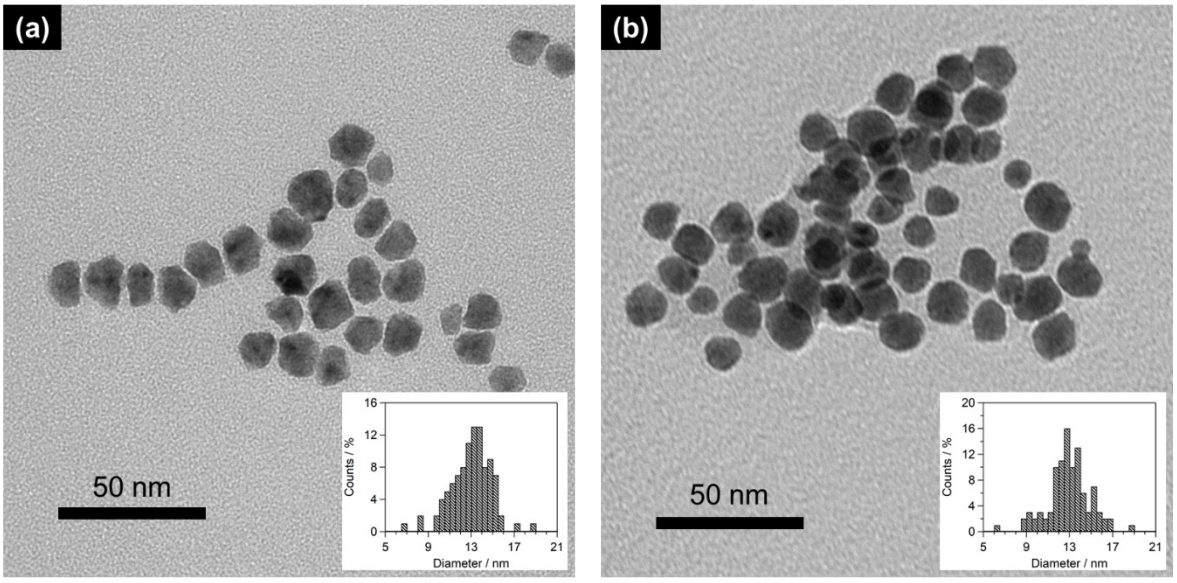

Figure S1 TEM images of (a) Pd–Ru NPs and (b) Pd–Ru–B NPs. The inset is the diameter distribution of each sample.

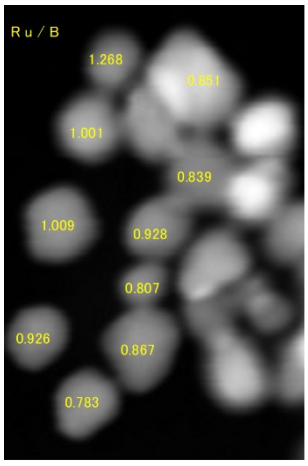

2. Compositional ratio from EELS spectra

Figure S2 Ru/B ratio of each particle calculated from EELS spectra. Combined with XRF results, the composition ratio of the obtained Pd–Ru–B NPs was approximately Pd:Ru:B = 1:1:1.

3. Structural characterization of Pd–Ru NPs

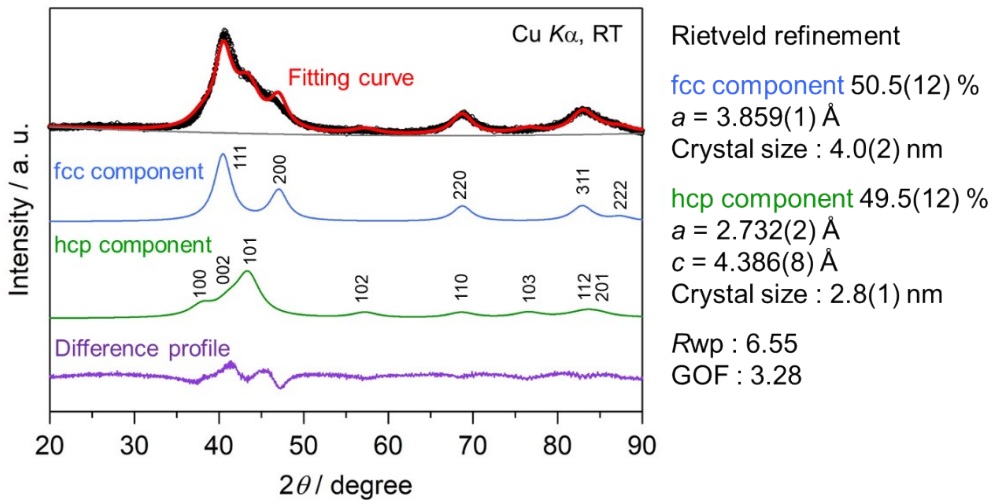

Figure S3 PXRD patterns of $Pd_{0.48}Ru_{0.52}$ NPs (black), and the corresponding Rietveld refinement. The blue, green, gray, purple and red lines show the fcc component, hcp component, background, difference profile and fitting curve, respectively. The radiation wavelength was 1.5406 Å.

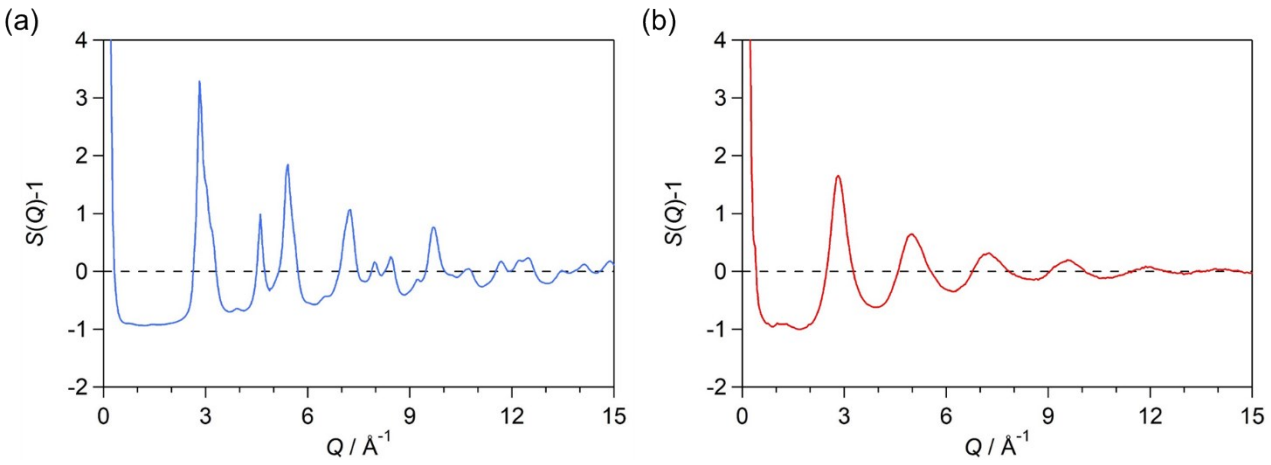

Figure S4 Total structure factor *S*(*Q*) of (a) Pd–Ru and (b) Pd–Ru–B NPs

Figure S5 shows a comparison of structure factor $S(Q)$ of Pd–Ru NPs between experimental and simulated profiles. In the experimental profile, there exists a peak at Q = 3.88 Å^{-1} (asterisk). The simulated fcc profile does not exhibit a peak at the same point. Furthermore, the simulated fcc profile has a distinct valley between peaks at Q = 4.59 Å^{-1} and Q = 5.39 Å^{-1}. However, the experimental one shows a shoulder at this Q range (open circle). These features indicate the existence of the hcp component in Pd–Ru NPs.

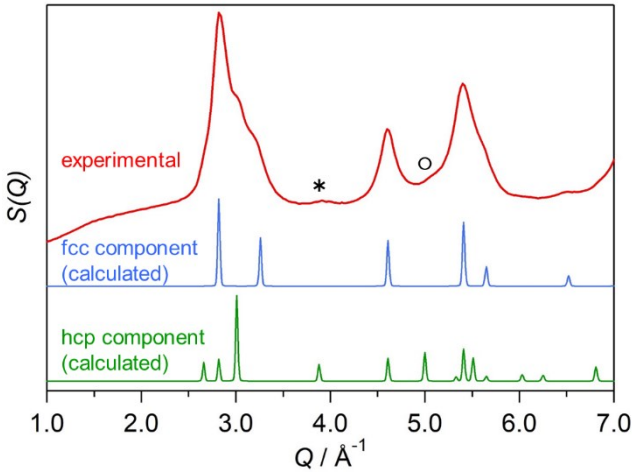

Figure S5 Comparison of experimental (red) and simulated structure factor $S(Q)$. The blue and green curves show the fcc and the hcp components, respectively.

Figure S6 shows a comparison of pair distribution function $G(r)$ of Pd–Ru NPs between experimental and simulated profiles. As seen in Figure S6(a), in the case of the simulated fcc profile, there should be valleys at r = 5.11 Å (asterisk) and 6.64 Å (open circle). However, the experimental profile did not show sharp minima at those points. This result indicates the existence of the hcp structure of Pd–Ru NPs. Furthermore, as shown in Figure S6(b), five peaks in the range of 8–10 Å have comparable peak intensities in the case of the experimental profile. The simulated fcc profile exhibits a distinct difference in peak intensity among those five peaks located in the same r range. This feature of $G(r)$ also suggests a contribution of the hcp component of Pd–Ru NPs.

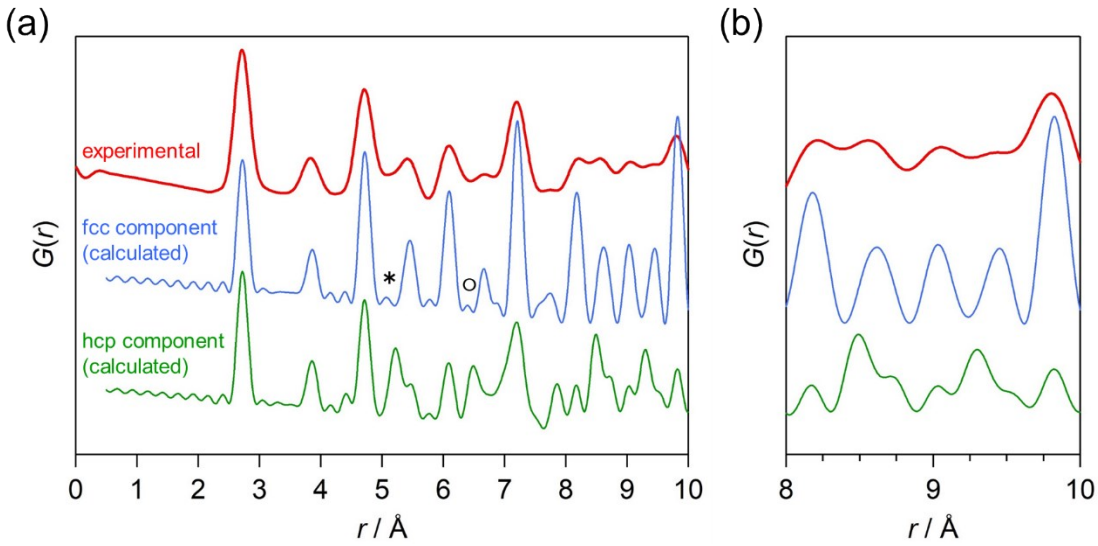

Figure S6 (a) Comparison of experimental (red) and simulated pair distribution function $G(r)$. The blue and green curves show the fcc and the hcp components, respectively. (b) A magnified image of the range of 8−10 Å in (a).

4. SAED pattern of Pd–Ru–B NPs

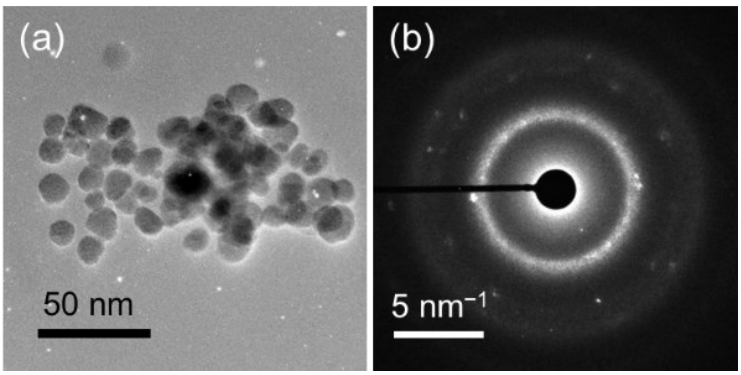

Figure S7 (a) Low-magnified TEM image and (b) corresponding SAED pattern of Pd–Ru–B NPs.

5. Atomic-resolution HAADF-STEM image and corresponding FFT pattern of Pd–Ru and Pd–Ru–B NPs

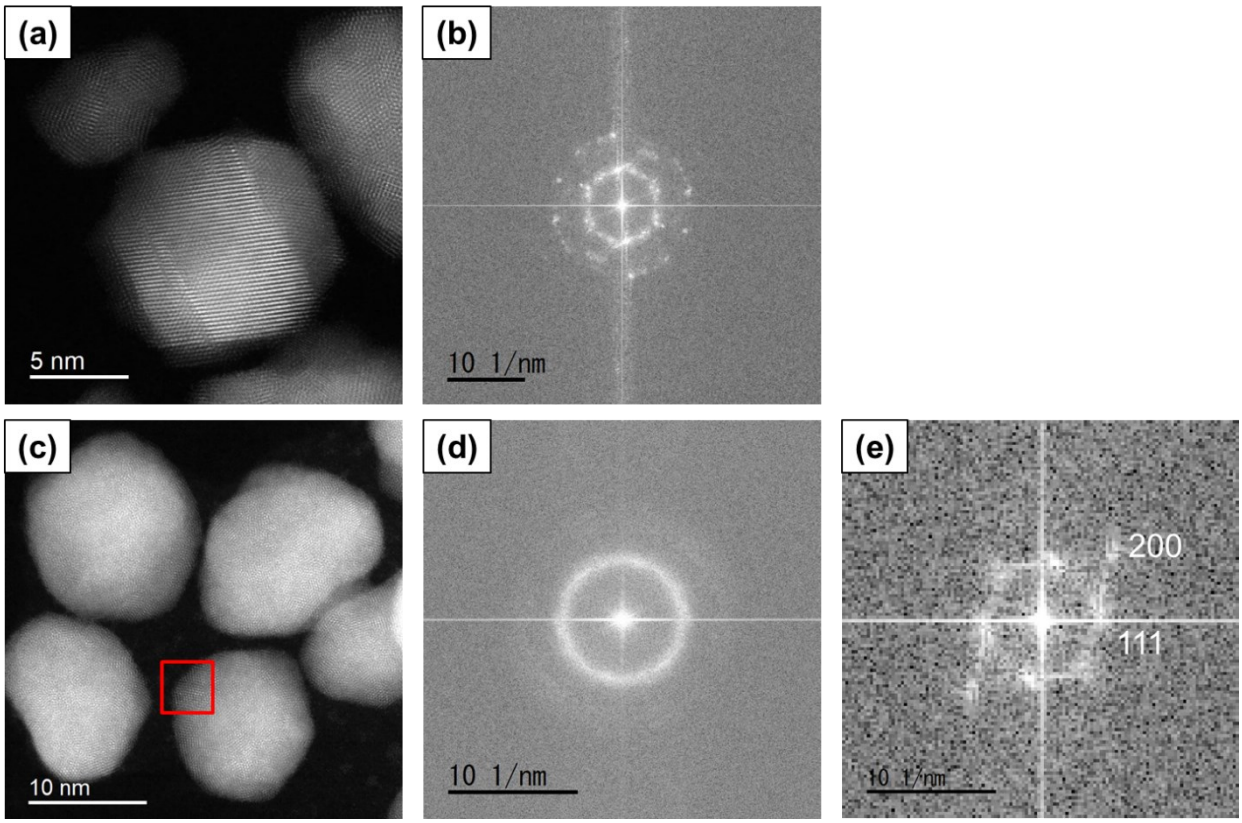

Figure S8 HAADF-STEM image (a) and corresponding FFT pattern (b) of Pd–Ru NPs. Those of Pd–Ru–B NPs are seen in (c) and (d), respectively. (e) FFT pattern obtained from the red square region in (c).

Figure S8 show HAADF-STEM images and corresponding FFT patterns of each sample. A clear lattice fringe is observable in Figure S8(a) and Fourier spots are shown in Figure S8(b), confirming the crystallinity of Pd–Ru NPs. On the other hand, most part of Pd–Ru–B NPs in the image of Figure S8(c) do not show clear lattice pattern and the corresponding FFT pattern from whole image of Figure S8(c) shows halo ring pattern in Figure S8(d). This suggest highly disordered atomic arrangement or even amorphous structure. Whereas, only small part of Pd–Ru–B NPs have clear lattice pattern such as indicated region with red square and the corresponding FFT patterns (such as Figure S8(e)) shows Fourier spots indicating existence of small crystals. Therefore, Pd–Ru–B NPs should be regarded as a composite from large amorphous body and small crystalline fraction, probably due to the gradual desorption of B atoms.

6. X-ray absorption near-edge structure (XANES) spectra of Pd–Ru and Pd–Ru–B NPs

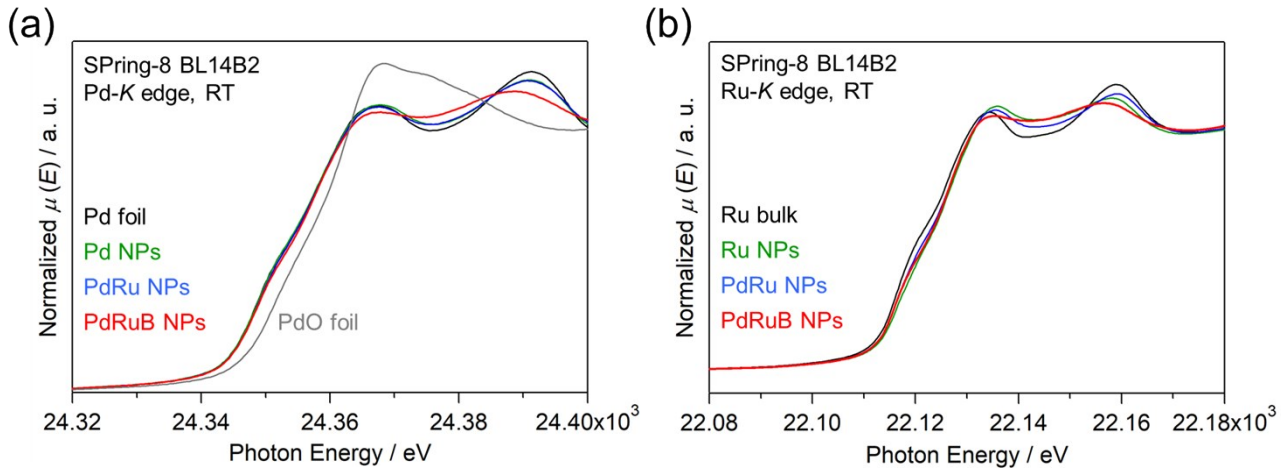

Figure S9 (a) Pd-*K* edge and (b) Ru-*K* edge XANES spectra in some kinds of NPs. The spectra of Pd foil, PdO foil, and Ru bulk are plotted as references.